PHOTONICS Research

Ultra-sharp silicon multimode waveguide bends based on double free-form curves

Shangsen Sun,[1,†] Zhiqiang Yang,[2,†] Juanli Wang,[1] Runsen Zhang,[1] Fengchun Zhang,[1] Ning Zhu,[1,5] Lei Wan,[3,6] and Zhaohui Li[2,4,7]

[1]Institute of Semiconductor Science and Technology, Guangdong Engineering Technology Research Center of Low Carbon and New Energy Materials, South China Normal University, Guangzhou 510631, China
[2]Guangdong Provincial Key Laboratory of Optoelectronic Information Processing Chips and Systems, Key Laboratory of Optoelectronic Materials and Technologies, School of Electrical and Information Technology, Sun Yat-sen University, Guangzhou 510275, China
[3]Department of Electronic Engineering, College of Information Science and Technology, Jinan University, Guangzhou 510632, China
[4]Southern Marine Science and Engineering Guangdong Laboratory (Zhuhai), Zhuhai 519000, China
[5]e-mail: zhuning@scnu.edu.cn
[6]e-mail: wanlei@jnu.edu.cn
[7]e-mail: lzhh88@sysu.edu.cn

Received 18 October 2021; revised 1 April 2022; accepted 24 April 2022; posted 25 April 2022 (Doc. ID 445529); published 26 May 2022

Mode-division multiplexing (MDM) can greatly improve the capacity of information transmission. The multimode waveguide bend (MWB) with small size and high performance is of great significance for the on-chip MDM integrated system. In this paper, an MWB with high performance based on double free-form curves (DFFCs) is proposed and realized. The DFFC is a combination of a series of arcs optimized by the inverse design method. The fabrication of this MWB only needs one-step lithography and plasma etching and has a large fabrication tolerance. MWBs with effective radii of 6 μm and 10 μm are designed to support three modes and four modes, respectively. The proposed method gives the best overall performance considering both the effective bending radius and the transmission efficiency. The fabricated MWB with four mode channels has low excess losses and crosstalks below −21 dB in the wavelength range from 1520 to 1580 nm. It is expected that this design can play an important role in promoting the dense integration of multimode transmission systems.

https://doi.org/10.1364/PRJ.445529

1. INTRODUCTION

With the development of all kinds of data services, information technology is now facing an extreme challenge in requirements for the expansion of transmission capacity accommodated within a single optical fiber [1–5]. The newly proposed mode-division multiplexing (MDM) technology utilizes different modes in the same wavelength band, and the amount of carried information can be further increased by this method [6–9]. In order to compactly route the guided modes in the on-chip multimode communication system, many functional waveguide devices suitable for multimode manipulations have been reported, including tapers [10,11], mode converters [12,13], multimode waveguide crossings [14–17], and multimode waveguide bends (MWBs) [12,18]. It is well known that when the transmitted light passes through a conventional MWB with compact size, there will be serious inter-couplings between the original guided modes inside the straight waveguide and the distorted modes inside the bent waveguide [19], causing unignorable excess losses and inter-modal crosstalks. Besides, for all kinds of the multimode waveguides, higher order modes have weak optical field confinement and tend to require a larger bending radius to reduce the radiation losses. An optimized waveguide bend requires a larger bending radius to accommodate more modes. Therefore, the design of a bent waveguide with a small radius and supporting as many modes as possible is of great significance to the monolithic MDM system [20].

In recent years, many methods have been proposed to realize the sharp bending of on-chip silicon multimode waveguides. An ultra-sharp silicon MWB based on the meta-surface (grating-like) structures has been proposed. The nonuniform grating mode converter on the straight multimode waveguide converts the "straight modes" to the "bent modes" ahead of the bend by changing the effective refractive index of the straight waveguide [21]. By this method a subwavelength grating (SWG) waveguide supporting four modes is achieved with the effective radius of 45.8 μm. Alternatively, these SWG structures can be also used to compensate for the structural asymmetry in the sharp bending region and convert the "bent modes" back to "straight modes" in the bent waveguide. The proposed MWB with the SWG on the bending part can support four TE modes with a bending radius of only

20 μm [22]. However, the manufacturing processes of these SWG-assisted bends are rather complex, which raises the scattering loss as well as the cost to some extent. Using a specially designed curve as the bending part of an MWB is another way to reduce the effective radius, since a curve with gradually changing radius can greatly reduce the mode field mismatch at the waveguide junction. MWBs based on the Bezier curve supporting three TE modes and on the modified Euler curve supporting four TM modes are designed, with bending radii of 20 μm and 45 μm, respectively [23,24]. Although these kinds of devices usually provide better transmission efficiencies by avoiding the scattering from the subwavelength mode-converting structures, the sizes are limited by the mathematical functions of the curves. While all the designs mentioned above use arc or other curves to bend the light, total internal reflection (TIR) can also be utilized to redirect the light [25]. Based on this principle, multimode waveguide corner bend (MWCB) supporting up to 10 TE modes is reported with the effective radius of 35 μm. Unfortunately, the MWCB requires a long adiabatic taper, which potentially deteriorates the integration density of the device. Other design methods of MWBs such as using mode converters and Etalon lens have also been proposed, but the scalability to higher order modes may be the key problem limiting the applications of these methods [12,18].

Instead of solving the problems forward, some works based at least partially on inverse design methods have also been proposed. An MWB supporting four TE modes with an effective radius of 17 μm is presented with the help of the transformation optics (TO) method [26]. The TO method is to map the traditional waveguide bend in the physical space to the virtual space as a distorted graded index waveguide. The boundary shape of this distorted waveguide in the virtual space is inversely optimized for highly efficient multimode transmission by the quadratic approximation method, and is then mapped back to the physical space to acquire the final sharp bending with high performance. In our previous work, an ultra-compact 90° MWB based on the inverse design has also been proposed [27]. The special curve in this work optimized by the inverse design method is called the free-form curve. The curve is directly optimized for multimode transmission in the physical space. The proposed free-form curve is such a smooth curve that the curvature radius of every point on it can be defined freely without the constraint of any mathematical function, and it is set to be self-symmetric around the angular bisector for convenience. In practice it is discretized by a series of different arcs (the discretization number is $2D$ considering the symmetry), and each two adjacent arcs have the same tangent at the junction. A combination of the reasonable curvature radii with low propagation loss can be found for these arcs by using the inverse design algorithm [28–35]. The optimization method used here is called direct range search (DRS) by modifying the famous direct binary search (DBS) method [36], which has been widely used in the field of optical simulations. In this paper, instead of using the MWB with a constant waveguide width, the internal and external curves of the MWB are designed as independent free-form curves. MWBs with double free-form curves (DFFCs) have been designed with even smaller bending radii compared with MWBs with single free-form curves (SFFCs). The reason lies in the effects of the waveguide width on the transmission performance. When the width reduces, the asymmetry between the inner and outer radii of the bent waveguide also reduces. This is helpful to reduce the field asymmetry and consequently the effective bending radius of the MWBs. However, a smaller waveguide width may increase the radiation losses of those high order modes inside the bending region. Thus, there is a trade-off between the loss and crosstalk when changing the width of the bent waveguide. Both the radius and the width everywhere on the bent structure need to be optimized carefully by the inverse design algorithm to reach the optimal bending performance. For the sake of this goal, we demonstrate two designs of the proposed DFFC–MWB with equivalent radii of 6 μm and 10 μm to support three and four TE modes, respectively. The size of the DFFC–MWB with four modes is about 50% smaller than that in our previous work. A comparison of the experimental results is also presented.

2. DESIGN AND SIMULATIONS

As shown in Fig. 1, the MWB with an equivalent radius of 10 μm is composed of two free-form curves A and B. W_S is the width of the MWB, which is not a constant necessarily. The free-form curves are mirror-symmetrical along the angular bisector, and the whole segment number is set as $2D$ for both curves. The inset of Fig. 1 shows the inner free-form curve A consisting of a series of different curvature radii, with $D = 3$ for convenience of presentation. R_i is the curvature radius of the ith arc and should decrease monotonously from R_1 to R_D to shrink the overall bending radius. O_i is the center of the ith arc, and R_A is the equivalent radius of curve A. The outer curve B has the same structure but is composed of a series of different radii R_i'. The figure-of-merit (FOM) function is defined as follows: the device is based on the silicon-on-insulator (SOI)

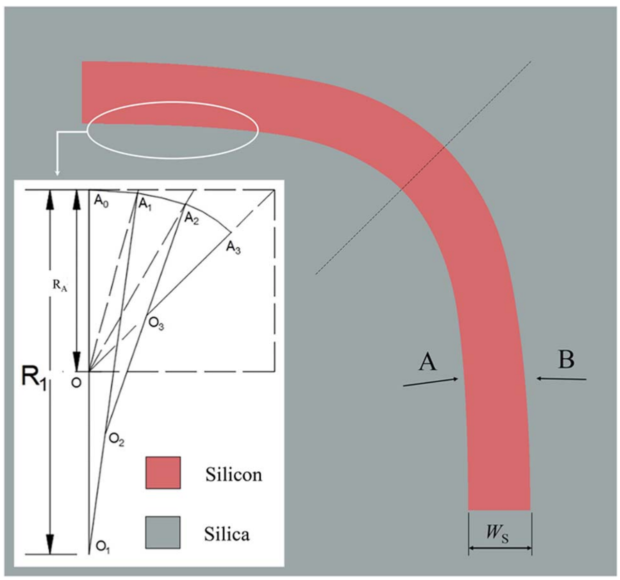

Fig. 1. Proposed MWB based on the DFFC design. DFFC consists of curve A and curve B, and W_S is the width of the MWB. The inset shows a schematic diagram of the change of curvature radius, and R_A is the equivalent radius of the free-form curve A.

platform for manufacturing compatibility [37,38]. The thickness of the silicon core layer is 220 nm, and the top layer could be air or silica. The 3D finite-difference time-domain (FDTD) method is used to calculate the FOM of the MWB. The FOM function is defined as

$$\mathrm{FOM} = 1 - \frac{1}{n}(1-\alpha)\sum_{I}^{n}(1-T_i) - \frac{1}{n}\alpha\sum_{I}^{n}X_i. \quad \textbf{(1)}$$

The excess loss and crosstalk of the ith mode are represented by T_i and X_i, respectively ($1 \le i \le n$). Depending on the emphasis of the simulation results, α is set to different values in the range of (0,1). Usually, α can be increased in the later stages of the simulations to further suppress the inter-mode crosstalks. Ideally, for the proposed device, the FOM is 1 for total transmission without any loss and crosstalk.

It is well known that setting some reasonable initial parameters is very important and time-saving for the inverse design [39,40]. In our previous work, R_i was defined as a random number from 0 to R_{MAX} ($R_{\mathrm{MAX}} = 5R_A$ typically, or more). By randomly selecting R_i one by one, it is somehow difficult to find all initial values that can be connected successfully from the input waveguide to the angular bisector, because sometimes the R_i decreases too fast to extend the curve properly. Thus, in this paper we use an improved method to obtain the initial values of all R_i:

$$R_i = R_{\mathrm{MAX}}[1 - \mathrm{rand}_i^m] \qquad 1 \le i \le D. \quad \textbf{(2)}$$

Herein the function rand returns a uniformly distributed random number from 0 to 1. The value of m is a real number from 0 to infinity. The higher the value of m, the greater the probability of large R_i. Then we can rearrange R_i by the sequence of their values to construct the curves. By selecting a proper m value, Eq. (2) tends to find values that can be used as the initial curve pattern efficiently. Moreover, the FOM of the initial curves determined by these R_i values also has a greater probability to reach a large value than those curves made of the R_i values picked randomly. A large FOM value of the initial waveguide structure can efficiently shorten the optimization time.

After curve A and curve B are obtained from Eq. (2), the width at the narrowest point of MWB is used as a screening criterion. Waveguides failing to support all the required modes with too small width at the narrowest point will be discarded. After comparing the values of the FOM, 100 groups of DFFCs with available performance are found. The segment radii normalized by the effective bending radius are shown in Fig. 2. At the following stage, the curves A and B will be reversely designed using the DRS algorithm described in Ref. [27]. In short, the optimization process can be defined as follows. Each R_i of curve A/B is varied in sequence, and the change will be discarded or kept depending on the FOM value. These searching procedures are repeated until the device's performance meets the criteria. For example, when R_1 is optimized, values from R_2 to R_{MAX} at an equal interval of 50 steps can be sampled for R_1 either in sequence or randomly. Each time the FOM of the MWB is calculated after a new value of R_1 is updated. If the FOM is greater than the initial value, the updated R_1 value is reserved, and the search for the next R_i (R_2 here) is then started. Otherwise, the FOM is recalculated

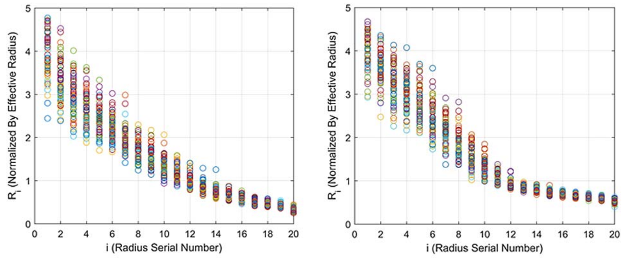

Fig. 2. Proper combinations of (a) curve A and (b) curve B are given. Here the ordinate represents a multiple of the equivalent radius.

after R_1 is changed again. If the FOM value is always smaller than the initial value when all the suitable values of R_1 have been tried, the search for the next R_i will be started anyway. The curve A can be obtained after the last radius R_D has been optimized. Similarly, the shape optimization of curve B will start in the same way. Repeat the above steps until the FOM of the proposed device is good enough. By this method, the MWB supporting three TE modes with an equivalent bending radius of 6 μm is designed as an example. The input waveguide width of the MWB is $W_S = 1.1$ μm to support three modes, and the segment number D is 20. Figures 3(a)–3(c) show the simulated optical field distributions in the designed MWB based on the DFFC for TE_0, TE_1, and TE_2 modes at the wavelength of 1.55 μm, respectively. It is easy to see that the guided waves for all three modes are almost unchanged at the output ports. The calculated transmission spectra of all modes in the device are shown in Figs. 3(d)–3(f). When operating at 1550 nm, the theoretical inter-modal crosstalks for three modes are all less than −31 dB and the excess losses are less than 0.2 dB. In the wide wavelength range of 1.5–1.6 μm, the inter-modal crosstalk is still very low (<24 dB) for each mode.

To support four mode channels, an MWB with an input waveguide width of $W_S = 1.48$ μm is designed. The equivalent radius of the MWB is increased to 10 μm, which can achieve sufficiently low inter-modal crosstalks and excess losses. The number of segments D is still selected as 20. After being optimized by the DRS algorithm, the proposed MWB gives the performances shown in Fig. 3. Figures 4(a)–4(d) give the simulated optical field distributions of this device for the first four TE modes with the operating wavelength of 1550 nm. The transmission spectra of the four-mode bends are shown in Figs. 4(e)–4(h). At the central wavelength, the bending losses for the four modes are calculated to be 0.019, 0.021, 0.023, and 0.129 dB, respectively. The device also has very low inter-modal crosstalk (<29 dB) for each mode at this wavelength. In the broadband from 1.5 to 1.6 μm, the highest inter-modal crosstalk is still below −23 dB.

In order to demonstrate the superiority of the DFFC design on the SFFC design in our previous work, an MWB based on the SFFC with the same effective radius and waveguide width is also simulated. The results are compared with each other in Table 1. For simplicity, only the worst cases of all crosstalk values at 1.55 μm are displayed in the table. It should be noted that these crosstalk values do not necessarily come from the

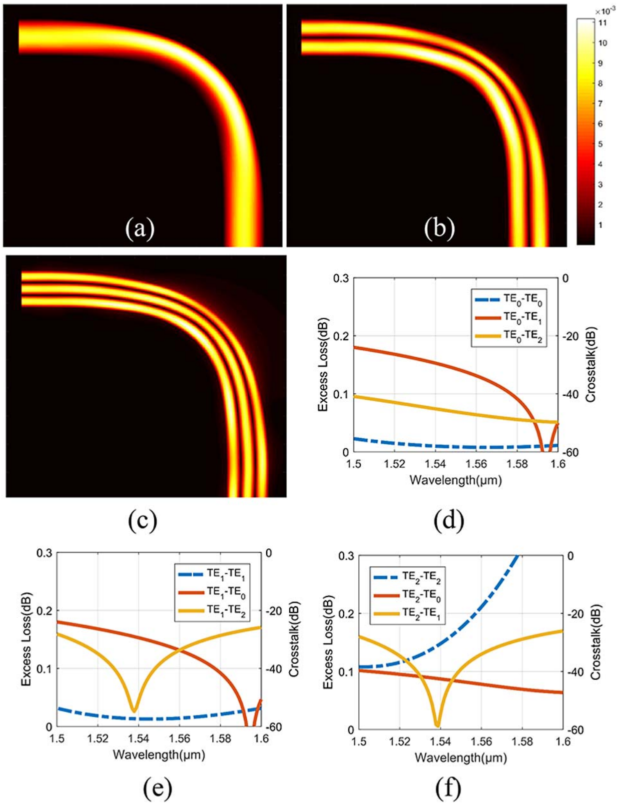

Fig. 3. Simulation results of the DFFC–MWB with an input width $W_S = 1.1$ μm. (a)–(c) Simulated optical field distributions in the designed MWB based on the DFFC with TE$_0$, TE$_1$, and TE$_2$ modes, respectively. (d)–(f) Calculated transmission spectra for three modes in the wavelength range of 1.5–1.6 μm. Herein the dotted line corresponds to the axis on the left, and the real line corresponds to the axis on the right.

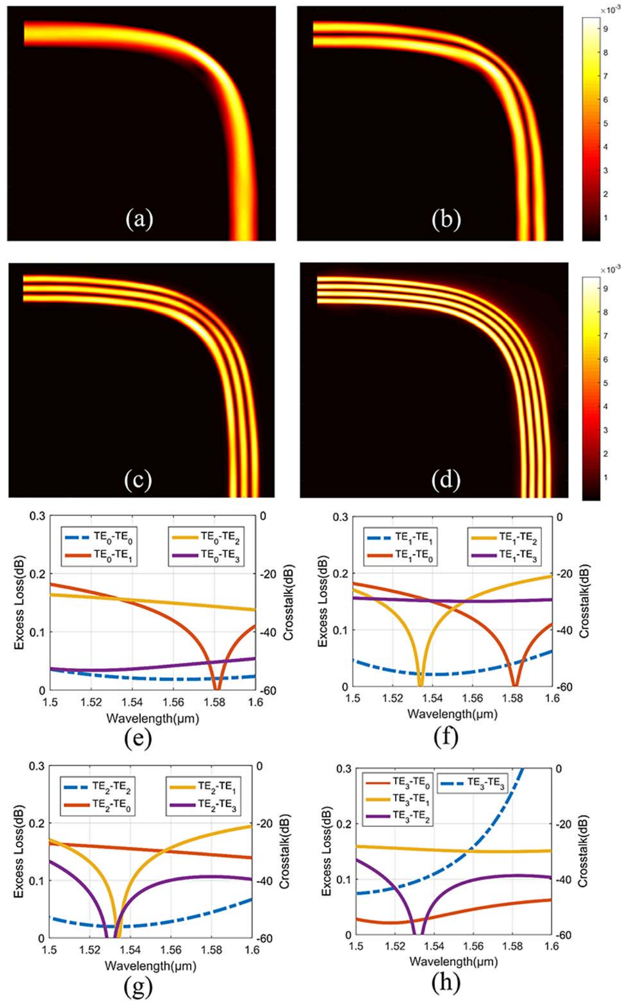

Fig. 4. Simulation results of the DFFC–MWB with an input width $W_S = 1.48$ μm and an equivalent radius of 10 μm. (a)–(d) Simulated optical field distributions in the device with four mode channels at 1.55 μm. (e)–(h) Calculated transmission spectra of the four-mode bent waveguide in the wavelength range of 1.5–1.6 μm. Herein the dotted line corresponds to the axis on the left, and the real line corresponds to the axis on the right.

same mode. As shown in Table 1, it is obvious that the performances of the DFFC designs are more balanced and better than those of the SFFC ones. The excess losses and crosstalks of the DFFC–MWBs are better than those of the SFFC–MWBs for almost all modes. Only the loss for the TE$_3$ mode of the SFFC design is slightly lower than that of the DFFC design. This is because the reduction of the waveguide width could increase the radiation loss of the high order mode, which slightly decreases the transmission of the highest order mode in the DFFC bend.

Last but not least, the fabrication tolerance should also be taken into account when selecting different MWB designs. For electron-beam lithography (EBL), the main fabrication error of an MWB device arises from the width deviation caused by the proximity effect in the exposure. In Fig. 5, we give the effects from the width deviation on the excess loss and crosstalk of a four-mode MWB. Since the deviation is much smaller than the waveguide width, we set the deviation ΔW constant everywhere for the whole MWB device. The width error is introduced by increasing or decreasing the magnitude of $\Delta W/2$ to the original curvature radii of each segment on curves A and B. The value of ΔW varies from −80 to 80 nm with a step of 10 nm. Figure 5 shows the transmission efficiencies of all modes at 1.55 μm with varying ΔW up to ± 80 nm. The worst value of all the crosstalks is around −20 dB within an error range of ± 40 nm, which roughly gives the fabrication tolerance. This result shows the good fabrication tolerance of the method reported in this paper.

3. FABRICATION AND CHARACTERIZATION

The devices fabricated on the SOI platform are tested to verify the above simulation results. The thickness of the silicon core layer and the silica under cladding layer is 0.22 and 2 μm, respectively. The EBL is used to define the patterns, and inductively coupled plasma (ICP) dry etching is applied to transfer the patterns to the silicon core layer. The mode (de)multiplexers with four mode channels are composed of asymmetrical directional couplers (ADCs) to (de)multiplex all the required modes [21,27]. The TE$_0$ modes in the single mode waveguides

Table 1. Calculated Results Related to Different Device Parameters for Comparison[a]

Mode	W_S (μm)	Method	T_1	X_1	T_2	X_2	T_3	X_3	T_4	X_4
Three	1.1	DFFC	0.0084	−31.38	0.0128	−31.34	0.1746	−39.33	/	/
		SFFC	0.0080	−32.07	0.0168	−26.74	0.3398	−26.63	/	/
Four	1.48	DFFC	0.0191	−29.61	0.0219	−29.92	0.0231	−29.47	0.1291	−29.82
		SFFC	0.0415	−23.09	0.0386	−23.08	0.0318	−27.35	0.0619	−31.59

[a]DFFC, double free-form curve; SFFC, single free-form curve. The units of T_i and X_i are decibels.

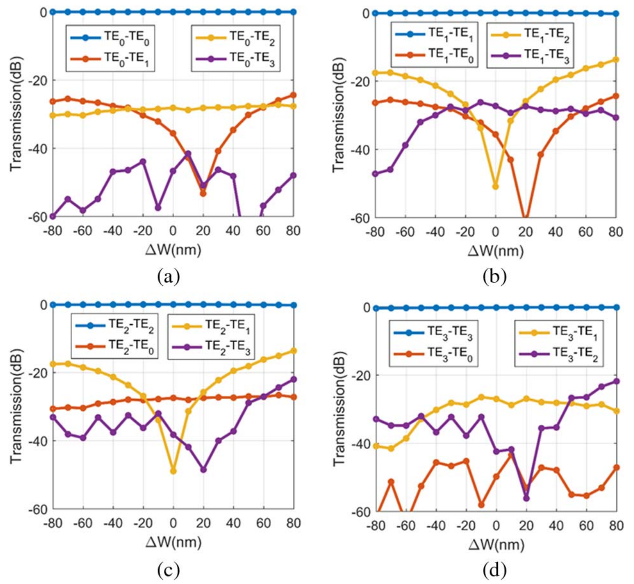

Fig. 5. Transmittance spectra of the MWB based on the DFFC with ΔW varying from −80 to 80 nm. (a)–(d) Transmission efficiencies of the four modes at 1550 nm. Simulation results show that this device has large fabrication tolerance.

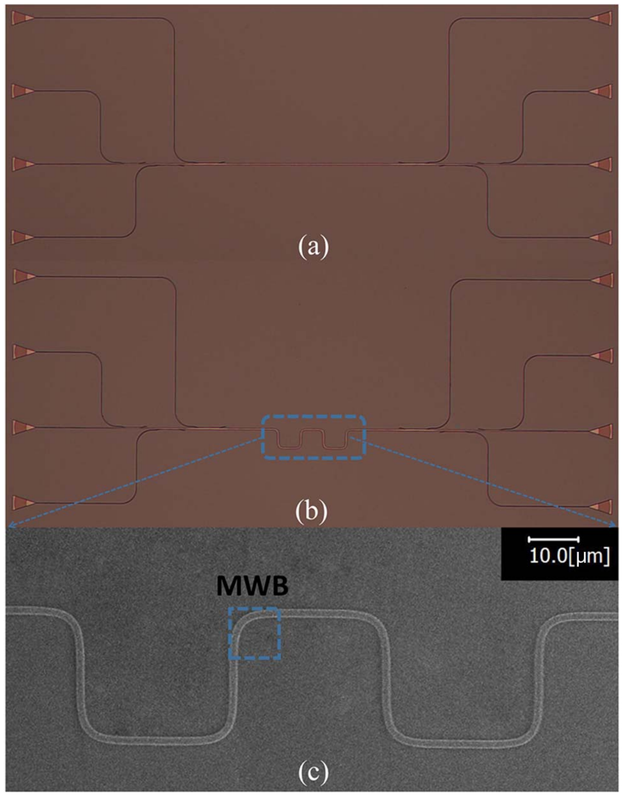

Fig. 6. Microscopic view of the fabricated silicon multimode bends with four mode channels. The multiplexer and demultiplexer are connected with (a) straight multimode waveguide or (b) eight cascaded 90° MWBs based on the DFFC. (c) SEM image of the cascaded MWBs.

are switched by the ADCs to desired high order TE modes. Figures 6(a) and 6(b) show the fabricated multiplexers and demultiplexers, which are connected to the straight multimode waveguide or the eight cascaded 90° MWBs based on the DFFC. A scanning electron microscope (SEM) picture of the cascaded MWBs is shown in Fig. 6(c). For comparison, the eight cascaded 90° MWBs based on the SFFC with the same equivalent radius and waveguide width are also fabricated on the same chip.

A tunable laser (Keysight 8164B) is used as well as a high-speed photodiode (Agilent 11982A) to measure the transmittance spectra of the fabricated devices. The insertion losses of the mode (de)multiplexers and the vertical grating couplers should be extracted from the transmission curve of each MWB [as shown in Figs. 6(a) and 6(b)]. The measured spectra of a single 90° four-mode bend based on the DFFC are shown in Figs. 7(a)–7(d). For the TE_0, TE_1, TE_2, and TE_3 modes, the waveguide bend has excess losses of 0.01, 0.05, 0.58, and 0.72 dB, respectively. The worst case of all crosstalk values is −25 dB. In a broadband wavelength range from 1520 to 1580 nm, the crosstalks between all modes are below −21 dB. Measurement results of the four-mode bend structure based on the SFFC are also shown in Figs. 7(e)–7(h). The crosstalk from TE_2 to TE_1 is about −15 dB at 1.55 μm. The performance of the four-mode bent waveguide based on the DFFC is obviously better than the one based on the SFFC with the same size, particularly when considering the crosstalk level. Due to the imperfectness in the fabrication, it is reasonable that the measured results are slightly lower than the simulated results.

Table 2 shows the comparison between the previously reported MWBs based on different structures and this work. It is obvious that both for the three-mode and four-mode MWBs, this work has better overall performance. To support the same number of TE modes, the MWBs based on the DFFC are almost half the size of those based on the SWGs [22]. The equivalent radius of the proposed device allowing high transmittance of three TE modes is only 6 μm, which is already close to the radius of the silicon single mode waveguide bend, and

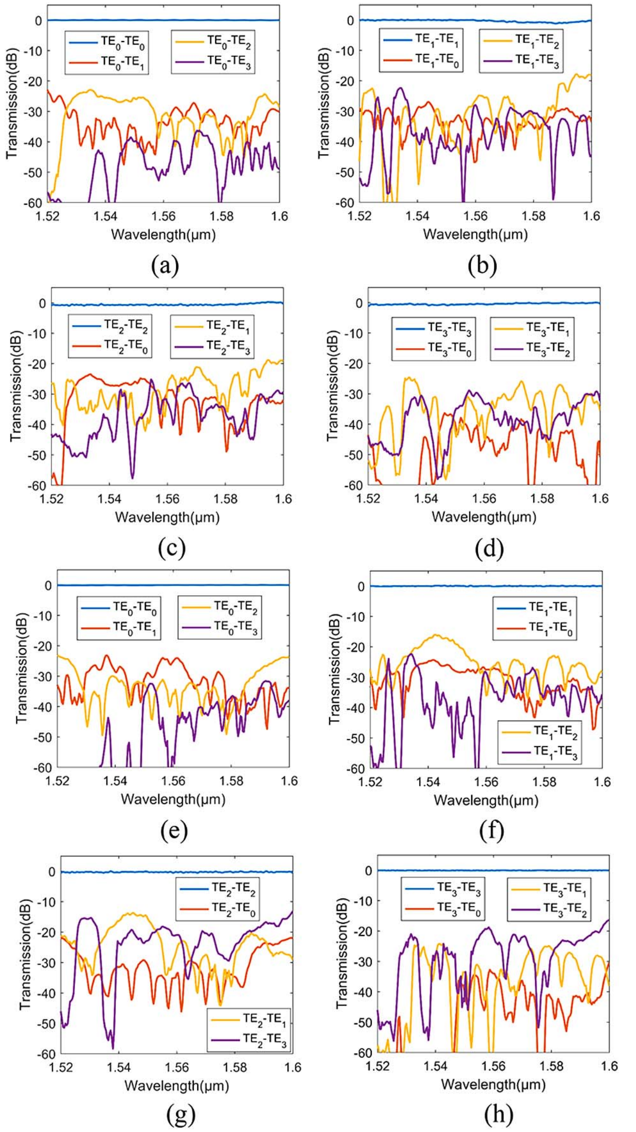

Fig. 7. Measured spectra of the normalized transmittances of a single four-mode waveguide bend. (a)–(h) Measurement results of a single 90° four-mode bend based on (a)–(d) DFFC or (e)–(h) SFFC.

that of the MWB with four-mode transmission is only 10 μm, which is the smallest four-mode bend to the best of our knowledge.

4. CONCLUSION

In this paper, we have proposed and demonstrated an MWB based on the DFFC. The improved DRS algorithm is used to optimize the shape of the DFFC. Unlike the Bezier curve or other mathematical functions, the DFFC utilizes two curves for which the changing of the segment radius is free instead of constraining in a certain mathematical form. The MWBs with effective radii of 6 μm and 10 μm are designed to support three modes and four modes, respectively. Theoretically, the bending losses of the three-mode MWB are calculated to be 0.008, 0.013, and 0.175 dB at 1.55 μm, for the TE_0, TE_1, and TE_2 modes, respectively. Each mode of the MWB has the intermodal crosstalk no more than −31 dB. Similarly, the MWB with four modes also has quite low excess losses (less than 0.12 dB for all modes) and low crosstalks (less than −29 dB). In the experiment, the measured four-mode MWB based on DFFC has excess losses of 0.01–0.72 dB and crosstalks less than −25 dB for the central wavelength, which is better than the MWB based on the method in our previous work. The method of this paper can be easily extended to more modes and is equally applicable to TM polarization. Besides, the MWB based on free-form curves can be easily applied to waveguides with other materials. The optimization procedures of the proposed device can be combined with other optimization algorithms, such as the artificial neural network and genetic algorithm, to improve the design speed. We believe the present design is of great help to increase the integration density of the on-chip multimode transmission systems.

Funding. Key Project in Broadband Communication and New Network of the Ministry of Science and Technology (MOST) (2019YFB1803904); National Natural Science Foundation of China (61805104, 62175095, U2001601); Natural Science Foundation of Guangdong Province (2020A1515010786); Science Foundation of Guangzhou

Table 2. Comparison of the Reported Results of Silicon Multimode Waveguide Bends[a]

Reference	Method	M_{ch}	R (μm)	EL (dB)		CT (dB)	
				Theory	Meas.	Theory	Meas.
[21]	SWG tapers	4	45.8	0.4	1	−20	−20
[22]	SWGs	3	10	0.5	0.7	−30	−20
		4	20	0.5	0.8	−26	−15
[23]	Euler curves	4	45	0.1	0.5	−25	−20
[24]	Bezier curves	3	20	0.2	/	−26	−23
[25]	Corner bend	2	7	0.18	0.53	−36	−15
		10	35	0.54	/	−24	/
[26]	TO-optimized	4	17	0.1	0.55	−20	−17
[27]	SFFC	3	9.35	0.04	0.2	−29	−25
This work	DFFC	3	6	0.17	/	−31	/
		4	10	0.13	0.72	−29	−25

[a]SWG, subwavelength grating; TO, transformation optics; SFFC, single free-form curve; DFFC, double free-form curve; EL, excess loss; CT, crosstalk; M_{ch}, mode-channel number. The units of EL and CT are decibels.

City (202102020593); China Postdoctoral Science Foundation (2021M693599).

Disclosures. The authors declare no conflicts of interest.

Data Availability. The data that support the findings of this study are available from the authors upon reasonable request.

†These authors contributed equally to this paper.

REFERENCES

1. L. Liu, Y. Ding, K. Yvind, and J. M. Hvam, "Silicon-on-insulator polarization splitting and rotating device for polarization diversity circuits," Opt. Express **19**, 12646–12651 (2011).
2. R. Chen, K. W. Ng, W. S. Ko, D. Parekh, F. Lu, T. Tran, K. Li, and C. Chang-Hasnain, "Nanophotonic integrated circuits from nanoresonators grown on silicon," Nat. Commun. **5**, 4325 (2014).
3. L. W. Luo, N. Ophir, C. P. Chen, L. H. Gabrielli, and M. Lipson, "WDM-compatible mode-division multiplexing on a silicon chip," Nat. Commun. **5**, 3069 (2014).
4. P. J. Winzer, "Making spatial multiplexing a reality," Nat. Photonics **8**, 345–348 (2014).
5. L.-T. Feng, M. Zhang, Z.-Y. Zhou, M. Li, X. Xiong, L. Yu, B.-S. Shi, G.-P. Guo, D.-X. Dai, and X.-F. Ren, "On-chip coherent conversion of photonic quantum entanglement between different degrees of freedom," Nat. Commun. **7**, 11985 (2016).
6. D. Dai, J. Wang, and Y. Shi, "Silicon mode (de)multiplexer enabling high capacity photonic networks-on-chip with a single-wavelength-carrier light," Opt. Lett. **38**, 1422–1424 (2013).
7. D. Dai, J. Wang, S. Chen, S. Wang, and S. He, "Monolithically integrated 64-channel silicon hybrid demultiplexer enabling simultaneous wavelength- and mode-division-multiplexing," Laser Photon. Rev. **9**, 339–344 (2015).
8. G. Chen, Y. Yu, and X. Zhang, "Monolithically mode division multiplexing photonic integrated circuit for large-capacity optical interconnection," Opt. Lett. **41**, 3543–3546 (2016).
9. J. Chen, Y. Yang, and N. Zhu, "Echelle grating based mode demultiplexer for vertical mode-division multiplexing," Opt. Express **24**, 24509–24516 (2016).
10. S. H. Badri and M. Gilarlue, "Ultrashort waveguide tapers based on Luneburg lens," J. Opt. **21**, 125802 (2019).
11. L. Sun and R. Zhang, "Metamaterial-based ultrashort multimode waveguide taper with low intermodal crosstalk," Opt. Express **29**, 7124–7133 (2021).
12. S. H. Badri, H. R. Saghai, and H. Soofi, "Polymer multimode waveguide bend based on a multilayered Eaton lens," Appl. Opt. **58**, 5219–5224 (2019).
13. H. Jia, H. Chen, T. Wang, H. Xiao, G. Ren, A. Mitchell, J. Yang, and Y. Tian, "Multi-channel parallel silicon mode-order converter for multimode on-chip optical switching," IEEE J. Sel. Top. Quantum Electron. **26**, 8302106 (2019).
14. W. Chang, L. Lu, X. Ren, D. Li, Z. Pan, M. Cheng, D. Liu, and M. Zhang, "Ultra compact dual-mode waveguide crossing based on subwavelength multimode-interference couplers," Photon. Res. **6**, 660–665 (2018).
15. S. Li, Y. Zhou, J. Dong, X. Zhang, E. Cassan, J. Hou, C. Yang, S. Chen, D. Gao, and H. Chen, "Universal multimode waveguide crossing based on transformation optics," Optica **5**, 1549–1556 (2018).
16. W. Chang, L. Lu, X. Ren, L. Lu, M. Cheng, D. Liu, and M. Zhang, "An ultra compact multimode waveguide crossing based on subwavelength asymmetric Y-junction," IEEE Photon. J. **10**, 4501008 (2018).
17. S. H. Badri, H. R. Saghai, and H. Soofi, "Polygonal Maxwell's fisheye lens via transformation optics as multimode waveguide crossing," J. Opt. **21**, 065102 (2019).
18. C. Sun, Y. Yu, G. Chen, and X. Zhang, "Ultra-compact bent multimode silicon waveguide with ultralow inter-mode crosstalk," Opt. Lett. **42**, 3004–3007 (2017).
19. L. H. Gabrielli, D. Liu, S. G. Johnson, and M. Lipson, "On-chip transformation optics for multimode waveguide bends," Nat. Commun. **3**, 1217 (2012).
20. L. Yang, T. Zhou, H. Jia, S. Yang, J. Ding, X. Fu, and L. Zhang, "General architectures for on-chip optical space and mode switching," Optica **5**, 180–187 (2018).
21. H. Xu and Y. Shi, "Ultra-sharp multi-mode waveguide bending assisted with metamaterial-based mode converters," Laser Photon. Rev. **12**, 1700240 (2018).
22. H. Wu, C. Li, L. Song, H. K. Tsang, J. E. Bowers, and D. Dai, "Ultra-sharp multimode waveguide bends with subwavelength gratings," Laser Photon. Rev. **13**, 1800119 (2019).
23. X. Jiang, W. Hao, and D. Dai, "Low-loss and low-crosstalk multimode waveguide bend on silicon," Opt. Express **26**, 17680–17689 (2018).
24. X. Wu, W. Zhou, D. Huang, Z. Zhang, Y. Wang, J. Bowers, and H. K. Tsang, "Low crosstalk bent multimode waveguide for on-chip mode-division multiplexing interconnects," in *CLEO: QELS_Fundamental Science* (Optical Society of America, 2018), paper JW2A.66.
25. Y. Wang and D. Dai, "Multimode silicon photonic waveguide corner-bend," Opt. Express **28**, 9062–9071 (2020).
26. S. Li, L. Cai, D. Gao, J. Dong, J. Hou, C. Yang, S. Chen, and X. Zhang, "Compact and broadband multimode waveguide bend by shape-optimizing with transformation optics," Photon. Res. **8**, 1843–1849 (2020).
27. S. Sun, P. Dong, F. Zhang, J. Wang, N. Zhu, and Y. Shi, "Inverse design of ultra-compact multimode waveguide bends based on the free-form curves," Laser Photon. Rev. **15**, 2100162 (2021).
28. S. Kirpatrick, C. D. Gelatt, and M. P. Vecchi, "Optimization by simulated annealing," in *Readings in Computer Vision* (1987), pp. 606–615.
29. A. Rickman, "The commercialization of silicon photonics," Nat. Photonics **8**, 579–582 (2014).
30. H.-L. Han, H. Li, X.-P. Zhang, A. Liu, T.-Y. Lin, Z. Chen, H.-B. Lv, M.-H. Lu, X.-P. Liu, and Y.-F. Chen, "High performance ultra-compact SOI waveguide crossing," Opt. Express **26**, 25602–25610 (2018).
31. S. Molesky, Z. Lin, A. Y. Piggott, W. Jin, J. Vucković, and A. W. Rodriguez, "Inverse design in nanophotonics," Nat. Photonics **12**, 659–670 (2018).
32. Y. Liu, K. Xu, S. Wang, W. Shen, H. Xie, Y. Wang, S. Xiao, Y. Yao, J. Du, and Z. He, "Arbitrarily routed mode-division multiplexed photonic circuits for dense integration," Nat. Commun. **10**, 3263 (2019).
33. Z. Liu, X. Liu, Z. Xiao, C. Lu, H.-Q. Wang, Y. Wu, X. Hu, Y.-C. Liu, H. Zhang, and X. Zhang, "Integrated nanophotonic wavelength router based on an intelligent algorithm," Optica **6**, 1367–1373 (2019).
34. K. Yao, R. Unni, and Y. Zheng, "Intelligent nanophotonics: merging photonics and artificial intelligence at the nanoscale," Nanophotonics **8**, 339–366 (2019).
35. Y. Augenstein and C. Rockstuhl, "Inverse design of nanophotonic devices with structural integrity," ACS Photon. **7**, 2190–2196 (2020).
36. M. A. Seldowitz, J. P. Allebach, and D. W. Sweeney, "Synthesis of digital holograms by direct binary search," Appl. Opt. **26**, 2788–2798 (1987).
37. M. Hochberg and T. Baehr-Jones, "Towards fabless silicon photonics," Nat. Photonics **4**, 492–494 (2010).
38. N. Hoppe, T. Föhn, P. Diersing, P. Scheck, W. Vogel, M. F. Rosa, M. Kaschel, M. Bach, and M. Berroth, "Design of an integrated dual-mode interferometer on 250 nm silicon-on-insulator," IEEE J. Sel. Top. Quantum Electron. **23**, 444–451 (2016).
39. B. Shen, P. Wang, R. Polson, and R. Menon, "An integrated-nanophotonics polarization beamsplitter with 2.4 × 2.4 μm² footprint," Nat. Photonics **9**, 378–382 (2015).
40. A. Y. Piggott, J. Lu, K. G. Lagoudakis, J. Petykiewicz, T. M. Babinec, and J. Vučković, "Inverse design and demonstration of a compact and broadband on-chip wavelength demultiplexer," Nat. Photonics **9**, 374–377 (2015).